Journal of Non-Newtonian Fluid Mechanics 179–180 (2012) 43–54

Contents lists available at SciVerse ScienceDirect

Journal of Non-Newtonian Fluid Mechanics

journal homepage: http://www.elsevier.com/locate/jnnfm

Inhomogeneous flows and shear banding formation in micellar solutions: Predictions of the BMP model

J.P. García-Sandoval [b,*], O. Manero [a], F. Bautista [b], J.E. Puig [b]

[a] Instituto de Investigaciones en Materiales, Universidad Nacional Autónoma de México, A.P. 70-360, México, D.F. 04510, Mexico
[b] Departamentos de Física e Ingeniería Química, Universidad de Guadalajara, Blvd. M. García-Barragán #1451, Guadalajara, Jal. 44300, Mexico

ARTICLE INFO

Article history:
Received 6 March 2012
Received in revised form 24 May 2012
Accepted 29 May 2012
Available online 12 June 2012

Keywords:
Inhomogeneous flows
BMP model
Wormlike micelles
Shear banding
Complex dynamics

ABSTRACT

The shear-banding flow in polymer-like micellar solutions is examined here with the Bautista–Manero–Puig (BMP) model. The expressions derived from the constitutive equations of the model, in addition to the conservation equations, are formulated for the case of inhomogeneous simple-shear flow. The resulting system of equations is hyperbolic, the solution of which can be found with the method of the characteristics. The characteristic trajectories associated to the system encompass a set of equations that is solved numerically. Here the actual flow initiation in a parallel plate rheometer is mimicked for both strain-controlled and stress controlled conditions, i.e., starting from rest, the velocity of the upper plate is allowed to increase stepwise to allow fully-developed flow after each velocity increment. In another case, the upper-plate velocity is allowed to decrease stepwise from a high shear rate down to low shear rates. When band formation is predicted, two or multiple bands are generated. Results include the phase portraits around the flow curve and for the confined fluid, predictions are given for the velocity, stress and fluidity fields as functions of both space and time. Moreover, it is shown that the values of the stress plateau and of the critical shear rates approach same values independently of the initial conditions and shear history for a given applied shear rate or shear stress. This result is obtained without the inclusion of gradient terms. An important result is that the model predicts the same stress plateau for forward and backward sweeps under strain controlled conditions and a discontinuity at the shear plateau for stress-controlled conditions.

1. Introduction

In a complex fluid, flow produces changes in its internal structure and induces fluctuations in the rheological properties. In complex fluids, the stress constitutive equation may be coupled to an evolution equation of a scalar representing the flow-induced modifications on the internal structure of the fluid (a variable such as the birefringence, the fluidity or the micellar length, in the particular case of giant micellar solutions).

The classical picture of banded flow describes the phenomenon by means of a flow curve with a maximum in the stress. Such non-monotonic flow curve is unstable, but steady flow can often be recovered by developing shear bands: layers of fluids with unequal strain rate but equal overall stress, their layers normal in the velocity gradient direction. The decreasing part of the flow curve is a region of coexistence between two bands, each one assigned to a critical shear rate. Assuming that the nature of the coexisting states does not vary as their amounts change, the steady-state is characterized by a stress plateau [1].

A constitutive relation describing the shear banding transition has been analyzed by Dhont [2,3]. The kinetics of the shear-banding was studied for parallel-plates geometry under controlled shear conditions. It was found that there exist multiple stationary states, depending on the initial state of the flow profile. Shear banding was predicted to occur not only when the system is initially unstable, but it can also be induced outside the unstable region when the amplitude of the initial perturbation is large enough. As a conclusion, the stationary state was not uniquely determined because it depended on the initial unstable perturbation. In this regard, two different initial conditions may lead to two different stationary banded structures in the case of parallel-plates geometry.

Greco and Ball [4] studied shear banding in start-up in Couette flow with the Johnson and Segalman (JS) model and demonstrated that the curvature produces a simple and well-controlled banded flow in contrast to planar flow, in which start-up calculations of similar local models give an uncontrolled number of bands. In addition, Georgiou and Vlassopoulos [5] studied the degeneracy of the JS model in Couette and Poiseuille flows, concluding that selection of a given banded steady state depends on the initial perturbation. Olmsted et al. [6] and Malkus et al. [7] studied the consequences of degeneracy for the history dependence of banded

* Corresponding author.
E-mail address: paulo.garcia@cucei.udg.mx (J.P. García-Sandoval).

0377-0257/$ - see front matter © 2012 Elsevier B.V. All rights reserved.
http://dx.doi.org/10.1016/j.jnnfm.2012.05.006

solutions using the original local JS model by imposing several flow histories. It was found that the apparent flow curves and the stress plateau depend on flow history. This is in contrast to experiments demonstrating that a unique selected shear stress plateau exists independently of flow history. An alternative to find a unique stress selection, non-local gradient terms have been heuristically added to the JS constitutive equation [6].

Although the non-local JS model has been useful to understand some features of the kinetics and stability of band formation, nevertheless there are two important setbacks of this model. The first is that the model itself cannot describe the breaking and reformation processes of the micellar systems under flow to enable an understanding of the relation between shear-band formation and microstructural evolution. The second one refers to the inability of the model to describe the evolution of the stress and normal stress differences under step-strain experiments in shear flow, and also, it gives unphysical responses in extensional flow [8]. Furthermore, the non-local JS model may predict reversal in the band ordering in Couette flows [6] in contrast to experimental data.

A model for wormlike micellar solutions involving scission and reforming of chains based on non-affine network theory and a discrete version of Cates theory was forwarded [8–10]. The homogeneous-flow model predicts non-monotonic flow curves as in previous versions of the BMP model. The inhomogeneous calculations predict a unique plateau stress and the progressive development of the shear bands in Couette flow.

Most of the published papers related to the comparison of the BMP model predictions with experiments were made for homogeneous flows, to analyze the advantages and limitations of the model to describe the wormlike micellar rheological response under flow. In this work, we solve the coupled differential equations for the stress, conservation of momentum and microstructure evolution (containing the underlying process of breakage and reformation of the micelles) to determine the local velocity field and the local kinematics of shear band formation, that lead to the resulting apparent flow curve. These coupled equations give rise to the inhomogeneous flow spatial inhomogeneities and shear banded states. The onset and temporal evolution of inhomogeneous states in steady and transient shear flows are further analyzed.

In this analysis, shear banding is triggered by the characteristics of the rate of deformation history at the inception of shear flow between two parallel plates, under the shear rate- or stress-controlled modes of operation. The upper plate moves with a stepwise increasing speed that departs from rest up to a certain prescribed value of the velocity. The decreasing stepwise mode departs from a reference state (high shear region). The dynamics and steady final banded state are analyzed for various values of the imposed velocity, with predictions of instabilities arising along the flow curve. Furthermore, predictions are given for the fluidity, stress and shear bands along the gap, as functions of distance and time.

We found that, contrary to the results obtained elsewhere, curvature of the flow cell is not a necessary condition to obtain a controlled number of bands, since these may be predicted in planar geometries, like parallel plates. Furthermore, we show that although the selection of banded states depends on the initial perturbations, the selected stress does not depend of flow history, in agreement with experiments. These results are obtained without the inclusion of gradient or non-local terms in the constitutive equations. In this paper we restrict ourselves to the linearized version of the BMP model, and leave for a future communication the inclusion of normal stresses.

2. Theoretical description

The following analysis is restricted to the linearized version of the BMP model in which normal stresses are negligible with small inertia. For simple-shear (where x is the direction of the macroscopic flow velocity, y is the direction of the velocity gradient and z is the direction of the vorticity), the set of equations of the BMP model are [11]:

$$\Sigma_{xy} = \sigma_{xy} + \eta_s \frac{\partial v_x}{\partial y} \tag{1}$$

$$\frac{1}{G_0\varphi}\frac{\partial \sigma_{xy}}{\partial t} = \frac{1}{\varphi}\frac{\partial v_x}{\partial y} - \sigma_{xy} \tag{2}$$

$$\frac{\partial \varphi}{\partial t} = \frac{1}{\lambda}(\varphi_0 - \varphi) + k_0\left(1 + \vartheta\frac{\partial v_x}{\partial y}\right)(\varphi_\infty - \varphi)\sigma_{xy}\frac{\partial v_x}{\partial y} \tag{3}$$

In this version of the model, we split the total shear stress Σ_{xy} into a non-uniform viscoelastic micellar contribution σ_{xy} added to a Newtonian solvent contribution with viscosity η_s. Here $\frac{\partial v_x}{\partial y}$ is the velocity gradient, φ is the fluidity or inverse of the shear viscosity (η^{-1}), $\varphi_0(\equiv \eta_0^{-1})$ is the fluidity at zero shear rate, $\varphi_\infty(\equiv \eta_\infty^{-1})$ is the fluidity at high shear rates, G_0 is the plateau shear modulus, λ is a structure relaxation time, k_0 can be interpreted as a kinetic parameter for structure breaking in the absence of shear flow, and ϑ is the shear banding intensity parameter. Conservation of linear momentum reads:

$$\rho\frac{\partial v_x}{\partial t} = \frac{\partial \Sigma_{xy}}{\partial y} \tag{4}$$

Eqs. (1)–(4) represent a closed set of time evolution equations for all the independent variables chosen to describe the behavior of complex fluids, in which the internal structure is modified by flow, and the non-equilibrium rheological properties which are functions of the kinetic process of reformation and modifications of the structure present at time t.

Alternative analyses [2,12] have considered a formulation in terms of the uniform shear stress, which comprises a non-uniform viscoelastic micellar contribution and a solvent contribution. In particular [12], the micellar stress follows a relaxation equation with length-dependent relaxation times with a steady homogeneous state, admitting a cubic equation of state. The micellar length itself follows an evolution equation related to the rates of micellar scission and recombination.

Solving for σ_{xy} in Eq. (2) and substituting the result into Eq. (1), we obtain the following expression in terms of the total stress:

$$\Sigma_{xy} - \eta_s\frac{\partial v_x}{\partial y} + \frac{1}{G_0\varphi}\frac{\partial}{\partial t}\left[\Sigma_{xy} - \eta_s\frac{\partial v_x}{\partial y}\right] = \frac{1}{\varphi}\frac{\partial v_x}{\partial y} \tag{5}$$

which may be arranged to give:

$$\Sigma_{xy} + \frac{1}{G_0\varphi}\frac{\partial}{\partial t}[\Sigma_{xy}] = \left(\frac{1}{\varphi} + \eta_s\right)\frac{\partial v_x}{\partial y} + \frac{\eta_s}{G_0\varphi}\frac{\partial}{\partial y}\left[\frac{\partial v_x}{\partial t}\right] \tag{6}$$

From conservation of momentum, Eq. (4), the total stress is given by:

$$\Sigma_{xy} + \frac{1}{G_0\varphi}\frac{\partial}{\partial t}[\Sigma_{xy}] = \left(\frac{1}{\varphi} + \eta_s\right)\frac{\partial v_x}{\partial y} + \frac{\eta_s/\rho}{G_0\varphi}\frac{\partial^2 \Sigma_{xy}}{\partial y^2} \tag{7}$$

The diffusive term in this equation is negligibly small (solvent kinematic viscosity times relaxation time) and decreases as the fluidity increases. In addition, it is assumed that the micellar viscosity is much larger than the solvent viscosity. In terms of the total stress, Eq. (3) is given by:

$$\frac{\partial \varphi}{\partial t} = \frac{1}{\lambda}(\varphi_0 - \varphi) + k_0\left(1 + \vartheta\frac{\partial v_x}{\partial y}\right)(\varphi_\infty - \varphi)\left(\Sigma_{xy} - \eta_s\frac{\partial v_x}{\partial y}\right)\frac{\partial v_x}{\partial y} \tag{8}$$

Here we neglect the squared gradient term times the solvent viscosity, which means that the dissipation produced by the solvent is

negligibly small compared to the dissipation of the system as a whole. The above argumentation implies that in the BMP equations written in terms of the total stress, the diffusive term therein arises naturally, but is negligibly small. In this regard, the solvent contribution has also been neglected in previous works [4].

Although the assumption of negligible solvent contribution is a good approximation in shear flow calculations; however, it is important to point out that in general flows is not valid. Indeed, Eq. (8) may be solved for the non-dimensional rate of dissipation under steady-state, i.e., $(\varphi-\varphi_0)/(\varphi_\infty-\varphi)$, which becomes unbounded when the fluidity approaches φ_∞. In addition, the extensional viscosity also diverges at high extension rates [13,14]. To resolve such inadequacy, here it is assumed that the total viscosity of the system is composed of the micellar and solvent contributions, such that $1/\varphi = 1/\varphi_m + \eta_s$; Eq. (7) is then written in terms of the micellar viscosity $1/\varphi_m$ and Eq. (8) contains the total viscosity. This assumption provides with a bounded dissipation rate and extensional viscosity, and also with additional elasticity at high shear rates, since the first normal stress is predicted to increase at high shear rates, in contrast to predictions of the modified model by Anderson et al. [14].

In the BMP model, the relation between the fluidity, relaxation time τ and micellar length n is:

$$\tau = \frac{1}{G_0\varphi} = \tau_0\left(\frac{n}{n_0}\right) \tag{9}$$

where τ_0 is the relaxation time when $\varphi = \varphi_0$. Substitution of Eq. (9) into Eq. (8), i.e., the evolution equation for the fluidity, yields an equation that can be expressed in terms of the average micellar length, which is the microstructural variable. The physical interpretation is that the micellar length n follows an evolution equation related to the breakage and reformation process of the micelles. This equation itself is coupled to the total stress, which contains the non-uniform micellar contribution.

Other models also couple the stress constitutive equation to an evolution equation for the structure variable. One of them [15] is a one-dimensional model that is essentially the same as Eqs. (2) and (3), except that Eq. (3) for the fluidity is replaced by the expression: $\partial\varphi/\partial t = -f(\varphi) + h(\varphi)\sigma\dot{\gamma} + D[\partial^2\varphi/\partial z^2]$, where f and h are non-linear functions of the fluidity. Eqs. (4), (7) and (8) are subjected to the boundary conditions:

$$v_x(t,0) = 0 \text{ and } v_x(t,L) = v_L(t) \tag{10}$$

where L is the gap between plates. The general initial conditions are:

$$v_x(0,y) = f(y), \quad \Sigma_{xy}(0,y) = g(y) \text{ and } \varphi(0,y) = h(y), \tag{11}$$

where $v_L(t) \geqslant 0$ is the upper plate or surface velocity which may be a function of time, while $f(y)$, $g(y)$ and $h(y)$ are functions of space; however, in most of the cases, $f(y) = 0$, $g(y) = 0$ and $h(y) = \varphi_0$.

The steady state when the upper plate motion is constant, i.e., $v_x(t,L) = v_{L,ss}$, is obtained by solving the following equations:

$$\frac{\partial\Sigma_{xy,ss}(y)}{\partial y} = 0 \tag{12}$$

$$\dot{\gamma}_{ss}(y) = \varphi_{ss}(y)\Sigma_{xy,ss}(y) \tag{13}$$

$$0 = \varphi_0 - \varphi_{ss}(y) + k_0\lambda[1+\vartheta\dot{\gamma}_{ss}(y)][\varphi_\infty - \varphi_{ss}(y)]\Sigma_{xy,ss}(y)\dot{\gamma}_{ss}(y) \tag{14}$$

where the subscript ss means steady state, and $\dot{\gamma}_{ss}(y) = \frac{dv_{x,ss}(y)}{dy}$. It is important to point out that at the inception of flow the stress is a function of space and time by momentum conservation (Eq. (4)). At long times, under steady-state conditions, the stress approaches a value independent of time and position.

As pointed out by Dhont [2], under steady-state Eqs. (12)–(14) hold with the constriction imposed by the modified Maxwell equal-area construction [11,16], i.e.

$$\int_{\dot{\gamma}_1}^{\dot{\gamma}_3}(\Sigma_{xy,ss}\varphi_{ss} - \dot{\gamma}_{ss})d\dot{\gamma}_{ss} = 0 \tag{15}$$

which means that the dissipation below and above the plateau stress is equal. This determines the location of the plateau stress, $\Sigma_{xy,ss} \equiv \Sigma_p$. It is important to remark that the criterion given in Eq. (15) is not used in the calculations that follow. Indeed, from the equations of the model itself is possible to demonstrate, from the potential derived for the cubic BMP equation of the fluidity as a function of the stress, the equal minima in this potential corresponding to two of the roots of the cubic equation sets the location of the plateau (see Appendix A). This derivation does not require extra conditions, since it is entirely deduced from the model itself, and moreover, this construction agrees with the equal minima in the dissipation. Elsewhere [11,17] we have obtained predictions in agreement with experiments that demonstrate that the dissipated energy contains two equal minima, which is consistent with the equal area criterion. Moreover, Greco and Ball [4] suggested a variational principle that leads to a principle of minimum of the functional containing the shear rate in the shear-rate controlled case. This in turn leads to a selection of the stress plateau corresponding to the equal areas of the stress–shear rate curve, in analogy with the Maxwell construction in equilibrium thermodynamics. The equal minima in the dissipation, the variational approach and the equal-areas criterion are then consistent with each other.

Substitution of Eq. (13) into Eq. (14) gives:

$$0 = (\varphi_0 - \varphi_{ss})\varphi_{ss} + k_0\lambda(1+\vartheta\dot{\gamma}_{ss})(\varphi_\infty - \varphi_{ss})\dot{\gamma}_{ss}^2 \tag{16a}$$

Eq. (16a) is cubic in the shear rate, corresponding to a non-monotonic flow curve [5]. On the other hand, this equation is quadratic in φ_{ss} with real solution:

$$\varphi_{ss} = \frac{1}{2}\left[\varphi_0 - k_0\lambda(1+\vartheta\dot{\gamma}_{ss})\dot{\gamma}_{ss}^2\right] + \sqrt{\frac{1}{4}\left[\varphi_0 - k_0\lambda(1+\vartheta\dot{\gamma}_{ss})\dot{\gamma}_{ss}^2\right]^2 + k_0\lambda(1+\vartheta\dot{\gamma}_{ss})\dot{\gamma}_{ss}^2\varphi_\infty} \tag{16b}$$

Integrating Eq. (13) with the boundary conditions (10) produces:

$$v_{x,ss}(y) = \Sigma_p\int_0^y \varphi_{ss}dy, \tag{17a}$$

and with $y = L$,

$$v_{L,ss} = \Sigma_p\int_0^L \varphi_{ss}dy \tag{17b}$$

Eq. (17) renders two stable steady states, each one with fluidity φ_1 and φ_3, respectively, whereas the other one is unstable with fluidity φ_2. Eqs. (17a) and (17b) lead to:

$$v_{L,ss} = \Sigma_p L[\chi\varphi_{1,ss} + (1-\chi)\varphi_{3,ss}] = \chi\dot{\gamma}_{1,ss} + (1-\chi)\dot{\gamma}_{3,ss} \tag{18}$$

where χ is the spatial proportion with shear rate $\dot{\gamma}_{1,ss} = \varphi_{1,ss}\Sigma_p$ and $(1-\chi)$ is the spatial proportion with shear rate $\dot{\gamma}_{3,ss} = \varphi_{3,ss}\Sigma_p$. The global applied shear rate is $\dot{\gamma}_{L,ss} = v_{L,ss}/L$, thus the proportion existing among the bands is:

$$\chi = \frac{\dot{\gamma}_{3,ss} - \dot{\gamma}_{L,ss}}{\dot{\gamma}_{3,ss} - \dot{\gamma}_{1,ss}} \tag{19}$$

Taking the spatial derivative of Eq. (4), the time derivative of Eq. (7), and eliminating the derivatives of the velocity, we obtain the following equation for the stress:

$$\frac{\partial^2\Sigma_{xy}}{\partial t^2} = \theta^2\frac{\partial^2\Sigma_{xy}}{\partial y^2} - G_0\frac{\partial}{\partial t}(\varphi\Sigma_{xy}) \tag{20}$$

where $\theta = G_0/\rho$. At short times, the resulting wave equation implies the inception of an oscillatory pattern. As time proceeds, the diffusion character of the equations gradually becomes predominant.

Written in this form, this equation allows for solutions of both the wave equation and the diffusion equation, depending on the time scale. The coefficient θ, which is the velocity $\sqrt{G_0/\rho}$, governs the time scale and spatial dimension of the process.

It is important to point out that due to conservation of momentum, (Eq. (4)), and the flow history, $v_L(t)$, the spatial derivative of the shear stress on the upper plate cannot be zero. Hence, the boundary conditions needed to solve the system are

$$v_x(t,0) = 0, \quad v_x(t,L) = v_L(t),$$
$$\frac{\partial \Sigma_{xy}(t,0)}{\partial y} = 0, \quad \frac{\partial \Sigma_{xy}(t,L)}{\partial y} = \rho \frac{dv_L(t)}{dt}$$

Therefore, the spatial derivative of the shear stress at the upper plate is zero only when steady-state is reached. This implies that the boundary condition at the upper plate is also history-dependent, in contrast to alternative approaches [18] wherein the derivative of the viscoelastic stress is assumed zero at the moving plate. If this is so, additional conditions imposed at the interface necessitate the inclusion of non-local terms. In the present analysis we neglect gradient terms, assuming that a finite interfacial width would be important only in highly confined flows, which is not the case we are analyzing here.

3. Results

One of the main objectives of this analysis is to find the relation between the features of the shear flow produced at the initiation stage of motion and the resulting steady-state shear-banding patterns. For simulation purposes, the parameters for a 10 wt.% cetyltrimethylammonium tosylate (CTAT) wormlike micellar solution at 30 °C, reported elsewhere [11], were used. To proceed further, it is necessary to simulate the actual initiation of shear flow in a rheometer. This is accomplished by introducing motor dynamics linked to the action of a "controller". The motor dynamics are represented by the following relaxation equation:

$$\frac{dv_L(t)}{dt} = \frac{v_c(t) - v_L(t)}{\tau_m} \tag{21}$$

where $v_L(t)$ is the velocity at $y = L$ and τ_m the response time of the motor. Considering a Proportional-Integral (PI) controller, the velocity calculated by the control action, $v_c(t)$, may be expressed according to the following expressions [19]:

$$v_c(t) = sat\left[K_c\left(e(t) + \frac{1}{\tau_I}\int_0^t e(\lambda)d\lambda\right)\right] \tag{22}$$

where K_c, the proportional gain, and τ_I, the integration time, are the controller parameters, while the saturation function $sat[u] = \begin{cases} 0 & \text{if } u < 0 \\ u & \text{if } u \geqslant 0 \end{cases}$ guaranteed that motor works only in one direction. The error for shear-rate controlled experiments is:

$$e(t) = \dot{\gamma}_{ref} - v_c(t)/L \tag{23}$$

where $\dot{\gamma}_{ref}$ is the shear-rate reference. In stress-controlled experiments, the error is:

$$e(t) = \sigma_{ref} - \sigma_{measured} \tag{24}$$

where σ_{ref} is the shear–stress reference.

In the following figures, results of various simulations are presented using the discretization method described in Appendix B with 500 spatial nodes. In these, the initial conditions considered are:

$$v_x|_{t=0} = 0, \quad \sigma|_{t=0} = 0, \quad \varphi|_{t=0} = \varphi_0 \tag{25}$$

In Fig. 1, the shear-rate controlled steady-state solutions for the stress as a function of shear rate are presented. Data represented with the symbol (+) were obtained increasing the shear rate from the system at rest; at time zero the controller was activated to regulate the shear rate. Reference shear-rates assigned as indicated in Fig. 1 were 0.4894, 7.88, 38.57, 188.7 and 3039 s^{-1} for points A, B, C, D and E, respectively; data represented by the symbol (○) were obtained with the initial reference shear-rate of 10,000 s^{-1} for decreasing shear-rates (every step in this mode lasted 1.25 min). Both simulation experiments depict a plateau stress for shear rates between 10 and 400 s^{-1}, locations of which agree with the equal-areas minima criterion of irreversible thermodynamics [11,16,20]. It is also important to remark that the system undergoes a meta-stable region at low shear rates before residing on the plateau (top-jumping scenario).

In the following figures (Figs. 2–6), the spatial and temporal dynamics before achieving steady states with or without banded regimes are shown for the controlled shear-rate mode. In every figure the constitutive curve is shown together with the temporal evolution of the shear stress versus shear rate for different spatial positions (a); arrows show the direction of variables evolution as time proceeds. In the remaining figures (b–d) the temporal and spatial evolution of the velocity profile, shear stress and fluidity are illustrated, respectively.

In Fig. 2, the reference shear rate (0.4894 s^{-1}) is smaller than the critical shear rate for the onset of shear banding (γ_{c1}). In Fig. 2a, trajectories of the stress and shear rate are spatially uniform. The steady-state is reached after 5 s, represented by point A in Fig. 1. The velocity, stress and fluidity (Fig. 2b–d) show a single band with a constant velocity profile, and a monotonically increasing stress and fluidity.

In Fig. 3, the shear rate corresponds to that of the local maximum of the stress (7.88 s^{-1}) within the meta-stable region (point B in Fig. 1). Again, the steady-state is reached after 5 s with a single velocity profile (Fig. 3b). In Fig. 3c, the stress shows an overshoot before achieving steady state. The fluidity, in turn, presents a monotonic increase up to steady state (Fig. 3d).

Fig. 4 shows the dynamics with a reference shear rate of 38.57 s^{-1}, corresponding to the plateau stress (point C in Fig. 1). In this case, a qualitative change occurs, since the time to attain steady-state has increased. Initially the trajectories of shear rate and stress are similar; notwithstanding they depart each other as time proceeds (Fig. 4a). The shear rate trajectories attain two different values corresponding to the meta-stable branches (binodals), one at low and another one at high shear rate with a bands

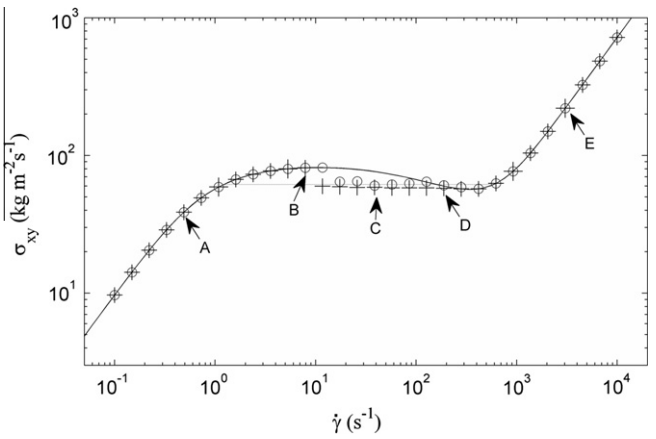

Fig. 1. Steady state constitutive curve obtained under controlled shear rate. Increasing shear rate starting from rest (+); decreasing shear rate starting from 10,000 s^{-1} (circles) Constitutive equation for the BMP model (Eq. (14)) (continuous line) and stress plateau calculated with the modified Maxwell equal-area construction (Eq. (15), dotted line).

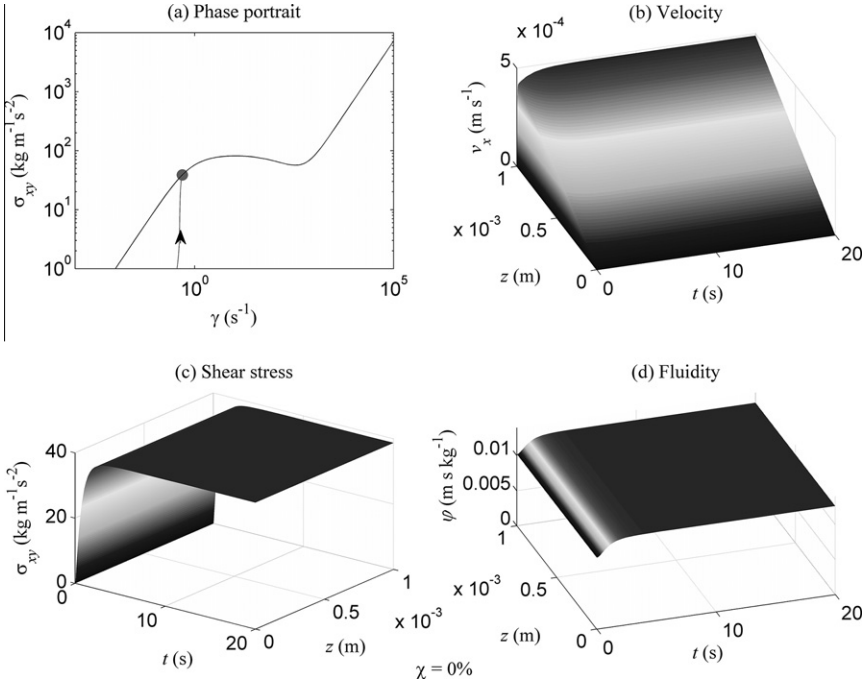

Fig. 2. Dynamics and steady-state under controlled shear rate. Reference shear rate is 0.4894 s^{-1}. Temporal trajectory of the stress and shear rate for various spatial positions (a); evolution of the velocity (b), stress (c) and fluidity (d) in space and time.

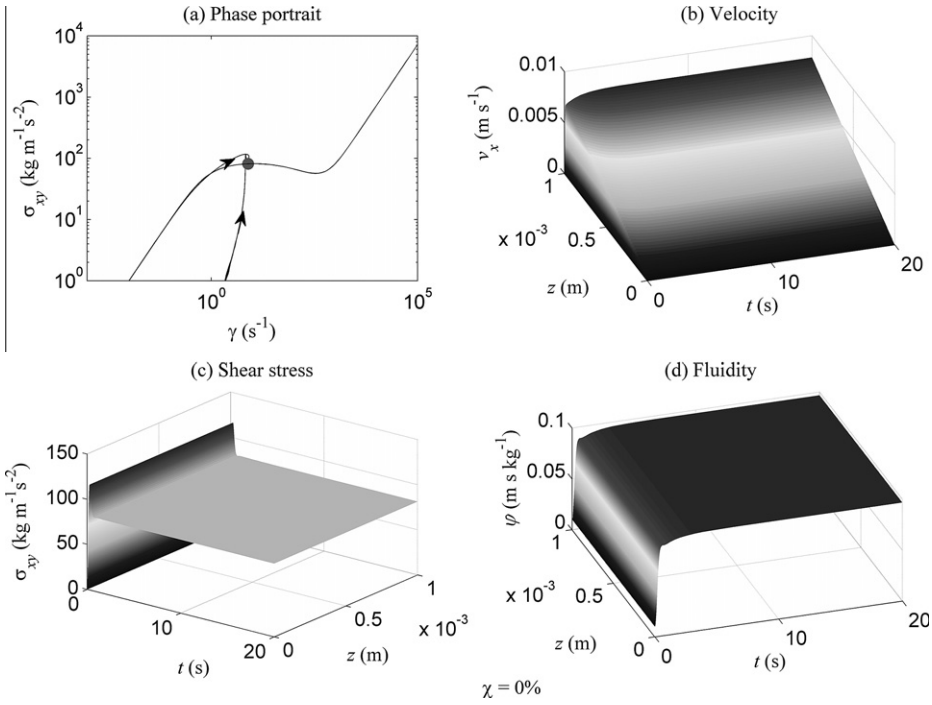

Fig. 3. Same as in Fig. 2. Reference shear rate is 7.88 s^{-1}.

proportion of 6% corresponding to the high-shear rate band. This is indicative of the presence of a shear-banding regime, wherein two bands are clearly seen in Fig. 4b, with two values of the velocity gradient. The stress trajectory remains essentially constant on the plateau stress. The stress shows an initial overshoot with slow attainment of the steady state (Fig. 4c), whereas the fluidity has two bands, a narrow one next to the moving plate and another wider one of low fluidity next to the stationary plate (Fig. 4d); the boundary between both regions reflects the change in velocity gradient between the bands.

In Fig. 5, the reference shear rate has now been increased to 188.7 s^{-1}, corresponding to that located at the extreme of the plateau (point D in Fig. 1). Results are similar to those of the previous figure, in that the shear rate and stress trajectories depart; the shear rate divides into two meta-stable branches, the binodals, and the shear stress attains steady values on the plateau

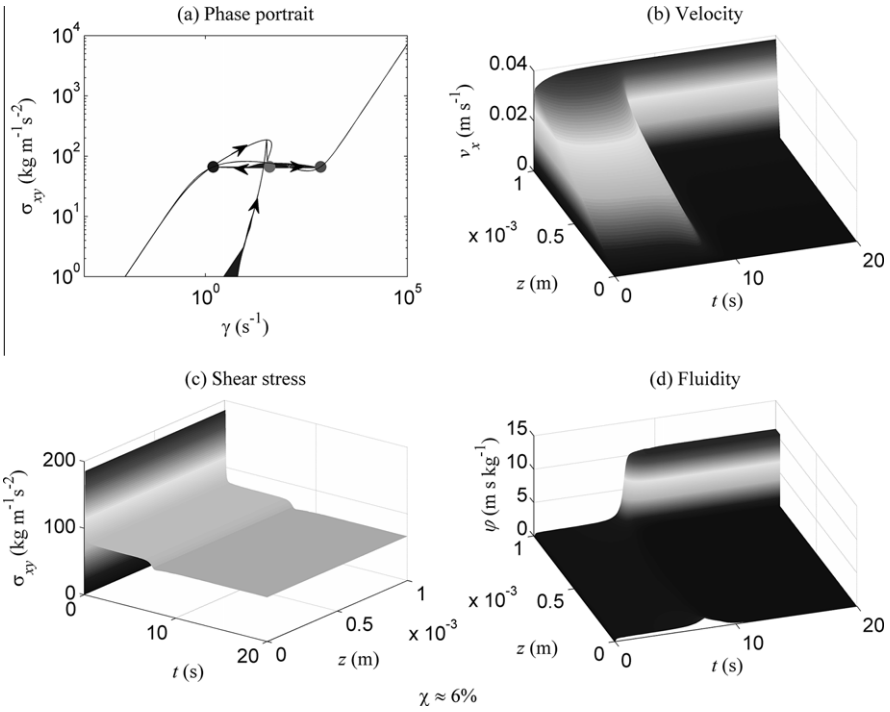

Fig. 4. Same as in Fig. 2. Reference shear rate is 38.57 s^{-1}.

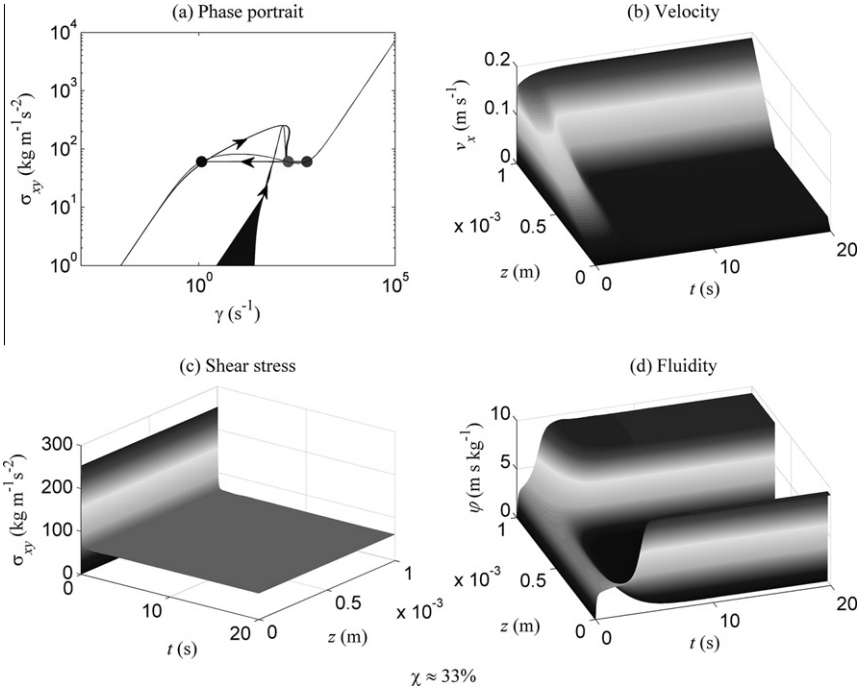

Fig. 5. Same as in Fig. 2. Reference shear rate is 188.7 s^{-1}.

(Fig. 5a). However, in this case the formation of three bands is apparent (Fig. 5b), two located next to the walls and another one located in the intermediate region. In addition, the proportion of the region of high fluidity (χ) has increased to approximately 33% (Fig. 5d).

Fig. 6 shows the results corresponding to the high shear rate branch (point E in Fig. 1). Although the trajectories of the dynamics depict increasing dispersion as compared to previous cases, the velocity profile exhibits a single velocity gradient (Fig. 6b), the stress shows an initial overshoot (Fig. 6c) and the fluidity attains steady state monotonically (Fig. 6d) in a short period of time.

The following figures (Figs. 7–10) illustrate results of the simulations under controlled stress. Once again, the points (+) denote increasing stress mode and circles represent decreasing stresses. In Fig. 7, steady state values are reproduced in which the stress is increased every minute stepwise; the procedure is repeated in the step-down mode for decreasing stresses. As observed, a discontinuity is apparent within the unstable region, in agreement with

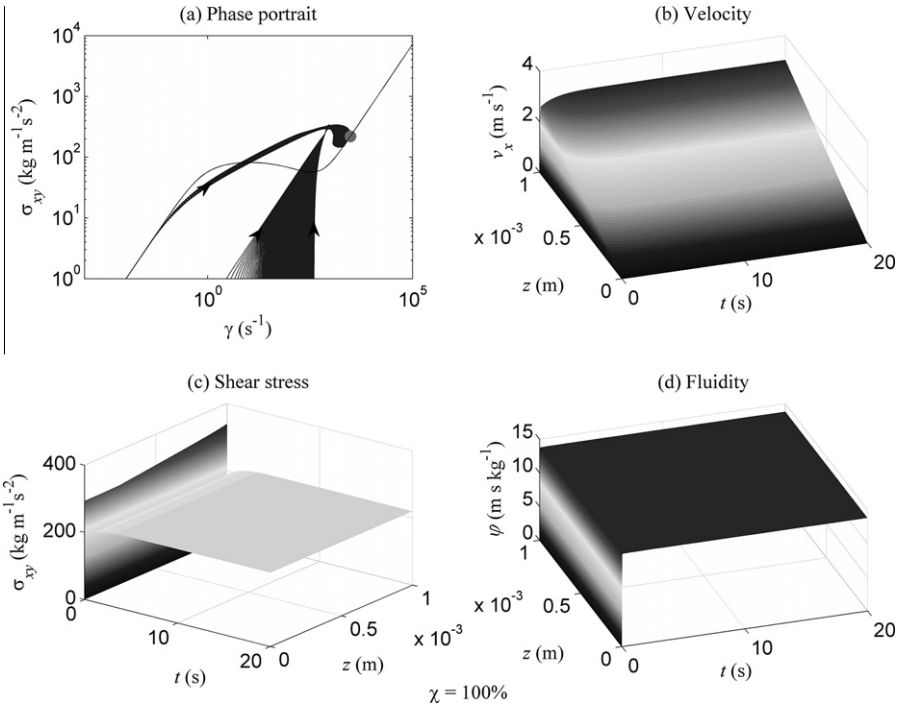

Fig. 6. Same as in Fig. 2. Reference shear rate is 3039 s^{-1}.

experimental results reported in the literature. Moreover, predicted stress values in the increasing and decreasing modes overlap along the whole flow curve.

Fig. 8 shows the dynamics when the reference stress is 60 Pa. The trajectories depict a stable steady region in the low shear rate extreme of the plateau. The velocity field is uniform, corresponding to a single shear rate (Fig. 8b). The initial overshoot in the stress and fluidity is followed by uniform steady state.

Fig. 9 shows different trajectories when the reference stress is changed from 85 to 60 Pa, after 5 s of dynamics duration. Here, the steady region at the extreme high shear rate of the plateau is attained in a short period of time. The results are similar to those of the previous figure, i.e., uniform velocity field and overshoot in the stress and fluidity, followed by uniform steady state, except that the velocity, stress and fluidity magnitudes are larger.

Fig. 10 shows qualitatively different results than those of the previous figures. Here, there is a programmed change in the reference stress (from 85 to 60 Pa) with different periods. The trajectories end at the two stable points at the extreme of the plateau in the meta-stable region (binodals). Formation of bands is apparent in the velocity profile (Fig. 10b), in which three bands are observed. This is reflected in the two regions of high fluidity next to the walls with a band proportion of approximately 67% and an intermediate region of low fluidity (Fig. 10d). Here it is important to point out that the distribution of bands (χ) is similar to that reported for Fig. 4, i.e., 6% of the high-shear rate band.

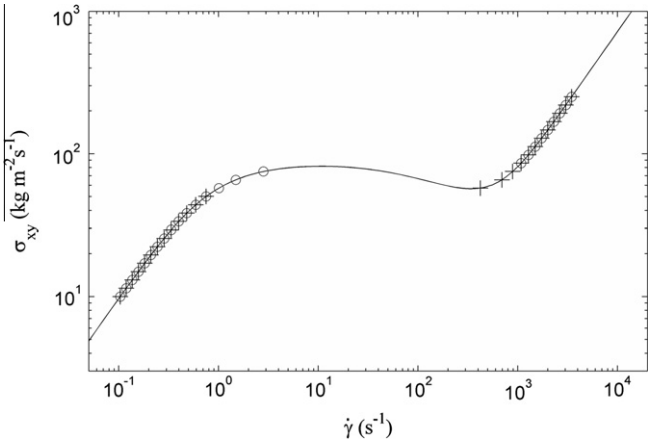

Fig. 7. Steady state constitutive curve obtained under controlled shear stress. Increasing stress starting from rest (+); decreasing stress starting from a high stress (circles).

4. Discussion

Under start-up of steady shear flow, the time evolution to steady state depends on the applied flow history, in such a way that various banded states are predicted when the initial flow conditions correspond to the stable or unstable regions of the underlying constitutive curve. However, the system selects a unique plateau independent of flow history, as shown in Fig. 1. The presence of a top-jumping scenario in the apparent equilibrium flow curve as well as different time-dependent trajectories have been observed in experiments with micellar solutions and in predictions with the non-local JS model or another non-linear models. Remarkably, experimental observations are consistent with the robustness of the stress plateau.

With reference to Fig. 1, it can be shown that in a linear plot circles and crosses overlap to within 5% in average, which is what is found in the dispersion of experimental data. In fact, the approach to steady state follows the actual operation of a rheometer and therefore, predictions should be compared with actual experimental data. The scatter found in experiments is of the same order as that of the predictions.

The BMP predictions show abrupt (albeit continuous) transitions at the interfaces of the bands that may be smoothed if gradient terms are added to the system of equations. We believe that these gradient terms may be included, not in the constitutive model but in a coupled equation describing the diffusion of mass,

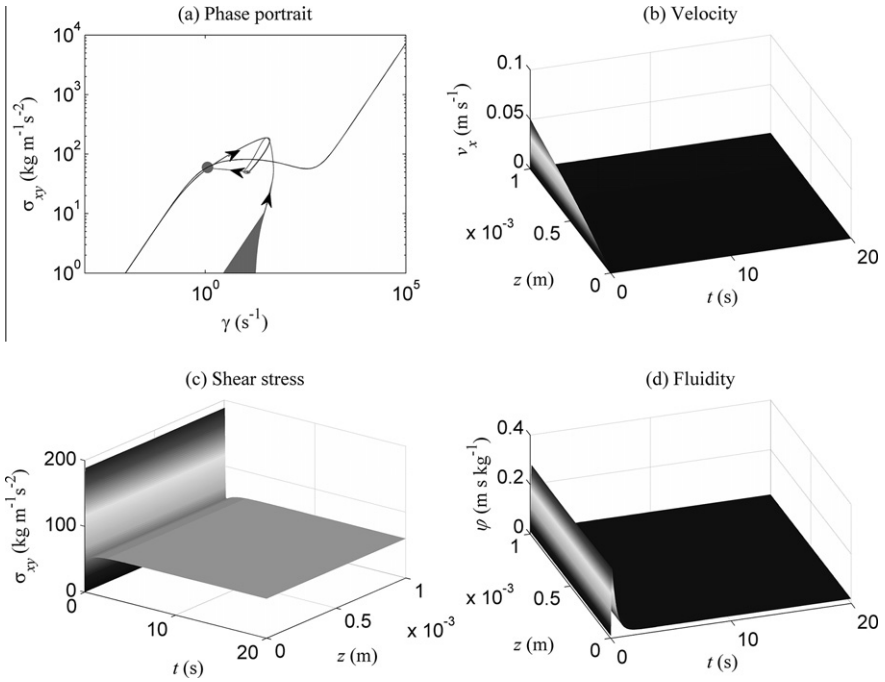

Fig. 8. Dynamics and steady-states under controlled shear stress. Temporal trajectory of the stress and shear rate for various spatial positions (a); evolution of the velocity (b), stress (c) and fluidity (d) in space and time. Final (steady state) stress reference is 60 Pa.

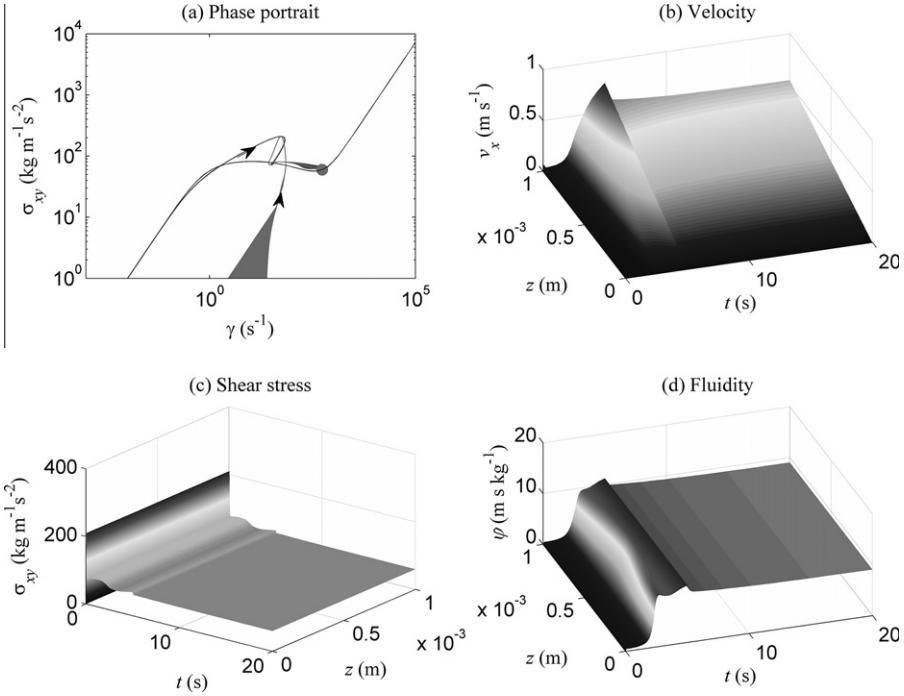

Fig. 9. Same as in Figure, with reference stress of 85 Pa for $t < 5$ s, and reference stress of 60 Pa for $t \geqslant 5$ s.

as suggested in a recent work on the generalized version of the model [17]. Indeed, this approach is similar to that studied by Yuan and Jupp [21] using a two-fluid model, which couples the viscoelastic stress and the diffusive fluid composition. In this approach, there is no need to introduce *ad hoc* diffusive stress terms into the constitutive equations. This model can select the steady-state stress in a physical way for non-monotonic constitutive equations under flow. This aspect is currently under investigation in our group.

Experimental evidence of three bands formation in micellar solutions is given in Manneville et al. [22] and Lerouge et al. [23] in rotational rheometers. In the first one, the banding structure is made up of three distinct regions: two layers located next to the walls separated by a mixed layer. This is similar to that obtained in Fig. 5b, wherein the formation of three bands is apparent, two located next to the walls and another one located in the intermediate region. In the second one, two high sheared bands next to the walls and a very weakly sheared central band are observed.

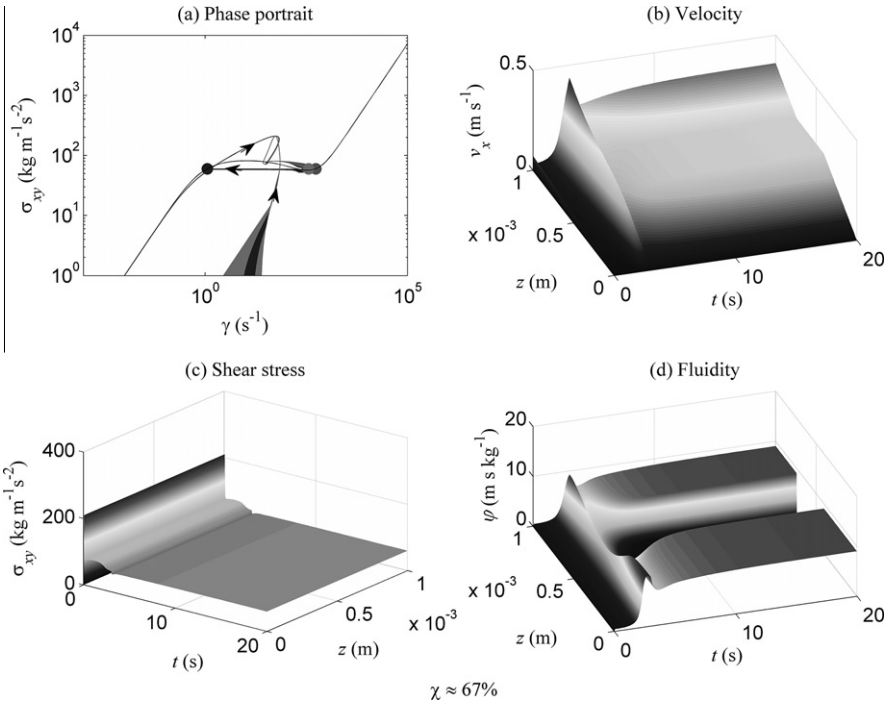

Fig. 10. Same as in Figure . Reference stress is 85 Pa for t<3 s and reference stress of 60 Pa for $t \geqslant 3$ s.

It is worth mentioning that these predictions can be compared with recent work on wormlike micellar systems using a network model which incorporates scission and reforming of the chains in homogeneous conditions [9]; later, this model was extended to analyze inhomogeneous flows [8,10]. Although diffusion was inherent to the kinetic theory description, selection of a unique plateau stress with developed shear banding was obtained past the initial transients showing progressively growth of the shear band across the gap. The evolution in the local stress and shear rate within a Couette fixture exhibits similar behavior to that exposed by the BMP model. When the imposed stress is within the multivalued region of the shear flow curve, the velocity profiles show shear-banding, with the high shear rate at the moving wall and the low shear rate at the fixed wall. This behavior is precisely that exposed in Fig. 4a–d. Moreover, the transient period to attain steady-state also predicts progressively growth of the shear bands across the gap.

Time dependent calculations in start-up of steady shear flow show that the velocity profiles between parallel plates and the total stress are coupled and evolve in a complex and non-monotonic form as the shear bands develop. The underlying non-monotonic constitutive flow curve in homogeneous flow leads to the development of shear bands in inhomogeneous flows. This is consistent with Particle Imaging Velocimetry (PIV) measurements in wormlike micellar solutions [24].

5. Concluding remarks

Results of the BMP model analysis presented here clearly demonstrate the importance of the initial rate of deformation history on the final banded state in shear-banding fluids. In the actual operation in a rheometer, where simple shear is usually generated in a Couette or cone-and-plate geometries, the tendency to produce banded flows depends not only on the properties of the fluids and flow regimes, but also on the initial conditions for inception of shear flow. Here, we analyzed shear rate- or stress-controlled modes. It is noteworthy that multiple bands may be generated depending on initial conditions. Previous analyses require non-local diffusive terms added to the constitutive equation [2,3,20] to generate the particular stable and unique plateau and banded states.

A novel prediction is that independently of the flow history, including increasing or decreasing shear rates, the same plateau stress is obtained. The BMP model also predicts a discontinuity in the stress plateau when measurements are done with stress-controlled conditions, in agreement with experimental data of the literature. The analytic part of the solution clearly shows that at short times the oscillatory pattern is in accord to a wave equation with propagation velocity θ. As time proceeds, the pattern becomes diffusive. An interesting issue is that the prediction of multiple bands did not require of non-local diffusive terms added to the constitutive equation. The linearized form of the BMP model predicts these complicated flow patterns.

Acknowledgement

We acknowledge the financial support from the National Council of Science and Technology through the Project 100195.

Appendix A

The cubic BMP equation for the fluidity as a function of the shear stress can be written as follows:

$$\varphi^3 - a\varphi^2 + b\varphi - c = -\lambda^* d\varphi/dt \tag{A.1}$$

where a, b and c are given by:

$$a = \varphi_\infty - \sigma_R^2/\mu \tag{A.2}$$

$$b = \varphi_\infty(1 - \sigma_R^2)/\mu \tag{A.3}$$

$$c = \varphi_\infty\varphi_0/\mu \tag{A.4}$$

Here,

$$\sigma_R = \sigma\sqrt{k\lambda\varphi_\infty} \tag{A.5}$$

and

$$\mu = \vartheta\sigma\sigma_R^2 \tag{A.6}$$

With increasing applied stress σ, a tends to an asymptotic value equal to φ_∞, while b and c decrease to zero. For low stresses, a and b may become negative. To this end, we redefine the fluidity to eliminate the quadratic term in (A.1) according to:

$$\phi = \varphi - a/3 \tag{A.7}$$

And then, we obtain for ϕ an equation in the standard form:

$$-\frac{d\phi}{d\tau} = \phi^3 + u\phi + v \tag{A.8}$$

where:

$$\begin{aligned} u &= b - a^2/3 \\ v &= ab/3 - 2a^3/27 - c \\ \tau &= t/\lambda \end{aligned} \tag{A.9}$$

Defining the potential V as:

$$V = \phi^4/4 + u\phi^2/2 + v\phi \tag{A.10}$$

Eq. (A.8) can be expressed as:

$$\frac{d\phi}{d\tau} = -\frac{dV}{d\phi} \tag{A.11}$$

Eq. (A.8) can have either one real root and a pair of complex conjugate roots, or three real roots $(\phi_{01}, \phi_{02}, \phi_{03})$. These two regimes are separated in the space of parameters (u, v) by the cubic equation:

$$4u^3 + 27v^2 = 0 \tag{A.12}$$

It turns out that in the regime of one single root the potential Eq. (A.10) describes a single minimum, while in the region of three real roots the potential describes two minima and one maximum. From a single steady-state, two steady-state solutions emerge. Once inside the domain corresponding to multiple steady-states, the two minima of V generally have different heights, except along a set of points (the plateau stress) when:

$$V(\phi_{01}) = V(\phi_{03}) \tag{A.13}$$

while ϕ_{02} is the value of ϕ at the maximum of V. It can be shown that the two states ϕ_{01}, ϕ_{03} are equally dominant attractors. This is truly the condition for the plateau stress.

In summary, as the applied stress reaches the value inside the region of multiple steady states, the condition Eq. (A.13) defines the loci of the plateau, where the attractors can define the location of the binodals $\dot{\gamma}(\phi_{01}), \dot{\gamma}(\phi_{03})$.

Appendix B. Numerical method

Using the dimensionless variables $\phi = \varphi/\varphi_0$, $\tau = G_0\,\varphi_0 t$, $Y = y/L$, $V_x = v_x/G_0\varphi_0 L$, and $\sigma = \Sigma_{xy}/G_0$, Eqs. (4), (7) and (8) become:

$$\frac{\partial V_x}{\partial \tau} = \theta^2 \frac{\partial \sigma}{\partial Y} \tag{B.1}$$

$$\frac{\partial \sigma}{\partial \tau} = \frac{\partial V_x}{\partial Y} - \sigma\phi \tag{B.2}$$

$$\frac{\partial \phi}{\partial \tau} = \frac{1}{\Lambda}(1-\phi) + \kappa\left(1 + \mu_1 \frac{\partial V_x}{\partial Y}\right)(\phi_\infty - \phi)\sigma\frac{\partial V_x}{\partial Y} \tag{B.3}$$

where $\kappa = G_0 k_0$, $\mu_1 = G_0\varphi_0\vartheta$, $\Lambda = G_0\ \lambda/\eta_0$ and $\theta = 1/\varphi_0 L\sqrt{G_0\rho} = \sqrt{v_0/G_0\varphi_0 L^2}$, $\tau \geqslant 0$ and $Y \in \{0, L\}$. The boundary conditions are now:

$$V_x(\tau, 0) = 0 \text{ and } V_x(\tau, 1) = V_L(\tau), \text{ with } V_L = v_L/G_0\varphi_0 L \tag{B.4}$$

and the initial conditions become:

$$V_x(0, Y) = f_1(Y), \quad \sigma(0, Y) = f_2(Y), \quad \phi(0, Y) = f_3(Y) \tag{B.5}$$

Also, from the conservation law (B.1) we obtain two more conditions

$$\frac{\partial \sigma(\tau, 0)}{\partial Y} = 0, \quad \frac{\partial \sigma(\tau, 1)}{\partial Y} = \frac{1}{\theta^2}\frac{dV_L(\tau)}{d\tau} \tag{B.6}$$

Defining:

$$X = \begin{pmatrix} V_x \\ \sigma \\ \phi \end{pmatrix}, \quad p = \begin{pmatrix} \partial V_x/\partial\tau \\ \partial\sigma/\partial\tau \\ \partial\phi/\partial\tau \end{pmatrix}, \quad q = \begin{pmatrix} \partial V_x/\partial Y \\ \partial\sigma/\partial Y \\ \partial\phi/\partial Y \end{pmatrix} \tag{B.7}$$

allows rewriting Eqs. (B.1), (B.2), (B.3) as:

$$0 = p_1 - \theta^2 q_2 \tag{B.8}$$

$$0 = p_2 - q_1 + X_2 X_3 \tag{B.9}$$

$$0 = p_3 - \kappa(1 + \mu_1 q_1)(\phi_\infty - X_3)X_2 q_1 + \frac{X_3 - 1}{\Lambda} \tag{B.10}$$

This system of equations has the form:

$$\frac{\partial X(t,y)}{\partial t} + M\left(X(t,y), \frac{\partial X(t,y)}{\partial y}\right) = 0 \tag{B.11}$$

with

$$M(X, q) = \begin{pmatrix} M_1 \\ M_2 \\ M_3 \end{pmatrix} = \begin{pmatrix} -\theta^2 q_2 \\ -q_1 + X_2 X_3 \\ -\kappa(1 + \mu_1 q_1)(\phi_\infty - X_3)X_2 q_1 + \frac{X_3 - 1}{\Lambda} \end{pmatrix} \tag{B.12}$$

With the method of characteristics [25–27] it is possible to show that the dimensionless mode, given by Eq. (B.11), the boundary conditions, Eqs. (B.4) and (B.6) as well as the initial conditions, Eq. (B.5), have three characteristic trajectories that are constant (see Fig. 11). To find the characteristic trajectories (ξ_1, ξ_2, ξ_3) we need to calculate the eigenvalues of the system of equations:

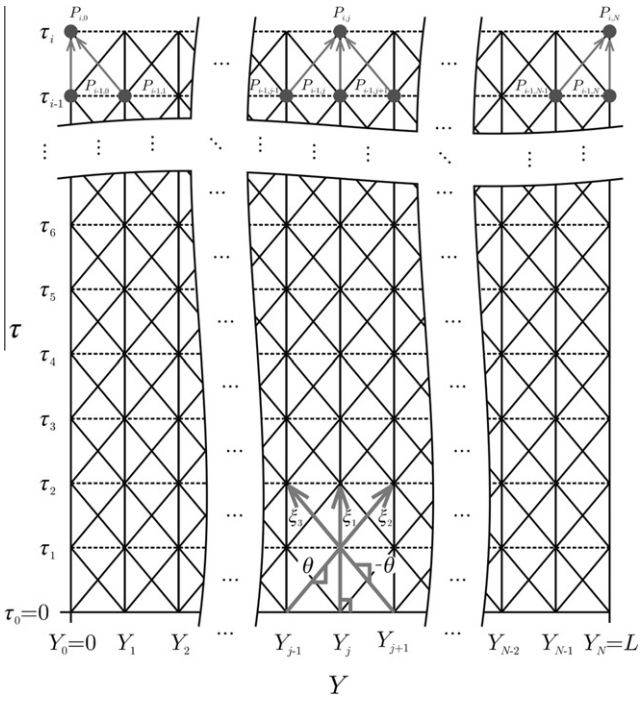

Fig. 11. Characteristic trajectories obtained from the solution of Eqs. (B.1), (B.2), (B.3) with boundary conditions (Eq. (B.4)) and initial conditions (Eq. (B.5)).

$$s\lambda_k - \sum_{j=1}^{n}\lambda_j \frac{\partial M_j}{\partial q_k} = 0, \quad k = 1,2,\ldots,n \tag{B.13}$$

which has a non-trivial solution for $\lambda = (\lambda_1, \lambda_2, \ldots, \lambda_n)$ if:

$$\begin{vmatrix} s & 1 & \kappa(1+2\mu_1 q_1)(\phi_\infty - X_3)X_2 \\ \theta^2 & s & 0 \\ 0 & 0 & s \end{vmatrix} = s(s^2-\theta^2) = 0 \tag{B.14}$$

Eq. (B.14) gives $s = 0, \pm\theta$. Since the roots are real, the system is hyperbolic, with three characteristic trajectories given by the following equations:

$$\xi_1 : y = y_0 \tag{B.15}$$

$$\xi_2 : y = y_0 + \theta(t - t_0) \tag{B.16}$$

$$\xi_3 : y = y_0 - \theta(t - t_0) \tag{B.17}$$

Following the method of the characteristics, and for the system (B.7), (B.8), (B.9), we seek solutions to the equation $\Omega_j\lambda = 0$ wherein, for Eq. (B.12), is given by:

$$\begin{pmatrix} s_j - \frac{\partial M_1}{\partial q_1} & -\frac{\partial M_2}{\partial q_1} & -\frac{\partial M_3}{\partial q_1} \\ -\frac{\partial M_1}{\partial q_2} & s_j - \frac{\partial M_2}{\partial q_2} & -\frac{\partial M_3}{\partial q_2} \\ -\frac{\partial M_1}{\partial q_3} & -\frac{\partial M_2}{\partial q_3} & s_j - \frac{\partial M_3}{\partial q_3} \\ \frac{\partial q_1}{\partial \xi_j} + \sum_{i=1}^{3}\frac{\partial M_1}{\partial X_i}q_i & \frac{\partial q_2}{\partial \xi_j} + \sum_{i=1}^{3}\frac{\partial M_2}{\partial X_i}q_i & \frac{\partial q_3}{\partial \xi_j} + \sum_{i=1}^{3}\frac{\partial M_3}{\partial X_i}q_i \\ \frac{\partial X_1}{\partial \xi_j} + M_1 - s_j q_1 & \frac{\partial X_2}{\partial \xi_j} + M_2 - s_j q_2 & \frac{\partial X_3}{\partial \xi_j} + M_3 - s_j q_3 \end{pmatrix} \begin{pmatrix} \lambda_1 \\ \lambda_2 \\ \lambda_3 \end{pmatrix} = 0 \tag{B.18}$$

Eq. (B.18) has a non-trivial solution if Eqs. (B.19c), (B.19d); Eqs. (B.20c), (B.20d) and (B.21c), (B.21d) hold.

$$\xi_1 \text{ direction}: \begin{cases} \frac{\partial \tau}{\partial \xi_1} = 1 & (a) \\ \frac{\partial Y}{\partial \xi_1} = 0 & (b) \\ \frac{\partial q_3}{\partial \xi_1} - \alpha(X,q)\frac{\partial q_2}{\partial \xi_1} = \beta_{11}(X,q) & (c) \\ \frac{\partial X_3}{\partial \xi_1} - \alpha(X,q)\frac{\partial X_2}{\partial \xi_1} = \beta_{12}(X,q) & (d) \end{cases} \tag{B.19}$$

$$\xi_2 \text{ direction}: \begin{cases} \frac{\partial \tau}{\partial \xi_2} = 1 & (a) \\ \frac{\partial Y}{\partial \xi_2} = \theta & (b) \\ \frac{\partial q_1}{\partial \xi_2} - \theta\frac{\partial q_2}{\partial \xi_2} = \beta_{21}(X,q) & (c) \\ \frac{\partial X_1}{\partial \xi_2} - \theta\frac{\partial X_2}{\partial \xi_2} = \beta_{22}(X,q) & (d) \end{cases} \tag{B.20}$$

$$\xi_3 \text{ direction}: \begin{cases} \frac{\partial \tau}{\partial \xi_3} = 1 & (a) \\ \frac{\partial Y}{\partial \xi_3} = -\theta & (b) \\ \frac{\partial q_1}{\partial \xi_3} + \theta\frac{\partial q_2}{\partial \xi_3} = \beta_{31}(X,q) & (c) \\ \frac{\partial X_1}{\partial \xi_3} + \theta\frac{\partial X_2}{\partial \xi_3} = \beta_{32}(X,q) & (d) \end{cases} \tag{B.21}$$

where

$$\alpha(X,q) = \kappa(1+2\mu_1 q_1)(\phi_\infty - \phi)X_2$$

$$\beta_{11}(X,q) = \alpha(X,q)(X_3 q_2 + X_2 q_3) - \kappa(1+\mu_1 q_1)[X_2 q_3 - (\phi_\infty - \phi)q_2]q_1 - \frac{1}{\Lambda}q_3$$

$$\beta_{12}(X,q) = \alpha(X,q)(X_2 X_3 - q_1) + \kappa(1+\mu_1 q_1)(\phi_\infty - \phi)X_2 q_1 + \frac{1}{\Lambda}(1 - X_3)$$

$$\beta_{21}(X,q) = \theta(X_2 q_3 + X_3 q_2)$$

$$\beta_{22}(X,q) = \theta X_2 X_3$$

$$\beta_{31}(X,q) = -\beta_{21}(X,q)$$

$$\beta_{32}(X,q) = -\beta_{22}(X,q)$$

Summarizing, the initial and boundary conditions are:

$$\text{Initial conditions} \begin{cases} X_1(0,Y) = f_1(Y)_- & (a) \\ X_2(0,Y) = f_2(Y) & (b) \\ X_3(0,Y) = f_3(Y) & (c) \\ q_1(0,Y) = \frac{df_1(Y)}{dY} & (d) \\ q_2(0,Y) = \frac{df_2(Y)}{dY} & (e) \\ q_3(0,Y) = \frac{df_3(Y)}{dY} & (f) \end{cases} \tag{B.22}$$

$$\text{Boundary conditions} \begin{cases} X_1(\tau,0) = 0 & (a) \\ V_x(\tau,1) = V_L(\tau) & (b) \\ q_2(\tau,0) = 0 & (c) \\ q_2(\tau,1) = \frac{1}{\theta}\frac{dV_L(\tau)}{d\tau} & (d) \end{cases} \tag{B.23}$$

The boundary conditions Eqs. (B.23a) and (B.23b) describe the conditions at the plates, while Eqs. (B.23c) and (B.23d) are the conditions of the stress spatial derivative on the plates, assuming the conservation Eq. (B.1).

According to Eqs. (B.19a), (B.19b), (B.19c), (B.19d), ϕ and σ are the variables associated with direction ξ_1, which in the space-time plane are the straight lines, $Y = Y_n$ for any $\tau > 0$, and $Y_n \in [0,1]$ (see Fig. 11). Furthermore, Eqs. (B.20a), (B.20b), (B.20c), (B.20d) and Eqs. (B.21a), (B.21b), (B.21c), (B.21d) reveal that V_x and σ propagate along the characteristic directions ξ_2 and ξ_3, which in the space-time plane are the straight lines $Y = Y_n + \theta(\tau - \tau_m)$ and $Y = Y_n - \theta(\tau - \tau_m)$ for any boundary or initial point (τ_m, Y_n) (see Fig. 11). To find the solution at the boundary $Y = 0$, we need only to seek the solution of Eqs. (B.19) and (B.21) together with conditions Eqs. (B.23a) and (B.23c) since the characteristic ξ_2 is not involved. Similarly, to find the solution at the boundary $Y = 1$, it is only necessary to seek the solution of Eqs. (B.19) and (B.20) together with conditions Eqs. (B.23b) and (B.23d) since the characteristic ξ_3 is not involved. Notice that these two directions, ξ_2 and ξ_3, are related to the velocity gradient and the stress (V_x and σ). In addition, since $\theta = 1/\varphi_0 L\sqrt{G_0\rho} = \sqrt{\upsilon_0/G_0\varphi_0 L^2}$, the waves for V_x and σ traveling along time and space depend on the gap, L, and θ can be considered a dimensionless number which is the ratio of the momentum diffusion (υ_0) to the viscoelastic diffusion ($G_0\varphi_0 L^2$). The third characteristic, ξ_1:$Y = Y_0$, given by Eq. (B.15), is independent of space and travels along time for constant axial points. This characteristic line is mainly related to stress and fluidity. For this reason, to analyze the behavior of the model we propose a numerical solution with a discretization method for axial derivatives, where for a given axial point (τ, Y_j) we approximate with central finite differences, given by:

$$\frac{\partial\sigma(\tau,Y_j)}{\partial Y} \approx \frac{\sigma(\tau,Y_{j+1}) - \sigma(\tau,Y_{j-1})}{Y_{j+1} - Y_{j-1}} \text{ and } \frac{\partial V_x(\tau,Y_j)}{\partial Y} \approx \frac{V_x(\tau,Y_{j+1}) - V_x(\tau,Y_{j-1})}{Y_{j+1} - Y_{j-1}},$$

while in each boundary we use forward and backward finite differences, respectively,

$$\frac{\partial\sigma(\tau,0)}{\partial Y} \approx \frac{\sigma(\tau,Y_1) - \sigma(\tau,0)}{Y_1} \text{ and } \frac{\partial V_x(\tau,0)}{\partial Y} \approx \frac{V_x(\tau,Y_1) - V_x(\tau,0)}{Y_1},$$

$$\frac{\partial\sigma(\tau,L)}{\partial Y} \approx \frac{\sigma(\tau,L) - \sigma(\tau,Y_{N-1})}{L - Y_{N-1}} \text{ and } \frac{\partial V_x(\tau,L)}{\partial Y} \approx \frac{V_x(\tau,L) - V_x(\tau,Y_{N-1})}{L - Y_{N-1}},$$

The set of Eqs. (B.1), (B.2), (B.3) is integrated along the characteristic trajectory ξ_1 for an specific number of axial points N with $Y_N = L$, where we define the variables $V_{x,j}(\tau) = V_x(\tau, Y_j)$, $\sigma_j(\tau) = \sigma(\tau, Y_j)$ and $\phi_j(\tau) = \phi(\tau, Y_j)$. The dynamics of the motor given in Eq. (22) as well as the controller in Eq. (23) with error given by Eq. (24) or Eq. (25), depending of the type of experiment considered, were also added to the simulation equations.

Appendix C. Supplementary material

Supplementary data associated with this article can be found, in the online version, at http://dx.doi.org/10.1016/j.jnnfm.2012.05.006.

References

[1] Giant Micelles, Properties and applications, in: R. Zana, E.W. Kaler (Eds.), Surfactant Science Series, vol. 140, CRC Press, Taylor & Francis, 2007 (Chapters 4 and 9).
[2] J.K.G. Dhont, A constitutive relation describing the shear banding transition, Phys. Rev. E 60 (1999) 4534–4544.
[3] J.K G. Dhont, W.J. Briels, Gradient and vorticity banding, Rheol. Acta 47 (2008) 257–281.
[4] F. Greco, R.C. Ball, Shear-band formation in a non-Newtonian fluid model with a constitutive instability, J. Non-Newtonian Fluid Mech. 69 (1997) 195–206.
[5] G.C. Georgiou, D. Vlassopoulos, On the stability of simple shear flow of a Johnson Segalman fluid, J. Non-Newton Fluid Mech. 75 (1998) 77–79.
[6] P.D. Olmsted, O. Radulescu, C.-Y.D. Lu, Johnson–Segalman model with a diffusion term in cylindrical Couette flow, J. Rheol. 44 (2000) 257–275.
[7] D.S. Malkus, J.S. Nohel, B.J. Plohr, Dynamics of shear flow of a non-Newtonian Fluid, J. Comput. Phys. 87 (1990) 464–487.
[8] L. Zhou, L.P. Cook, G.H. McKinley, Probing shear-banding transitions of a model entangled wormlike micellar solution using large amplitude oscillatory shearing (LAOS) deformations, J. Non-Newton. Fluid Mech. 165 (2010) 1462–1472.
[9] P.A. Vasquez, G.H. McKinley, L.P. Cook, A network scission model for wormlike micellar solutions. I. Model formulation and viscometric flow predictions, J. Non-Newton. Fluid Mech. 144 (2007) 122–139.
[10] L. Zhou, P.A. Vasquez, L.P. Cook, G.H. McKinley, Modeling the inhomogeneous response and formation of shear bands in steady and transient flows of entangled liquids, J. Rheol. 52 (2008) 591–623.
[11] F. Bautista, J.F.A. Soltero, O. Manero, J.E. Puig, Irreversible thermodynamics approach and modeling of shear-banding flow of wormlike micelles, J. Phys. Chem. B 106 (2002) 13018–13026.
[12] S.M. Fielding, P. Olmsted, Spatiotemporal oscillations and rheochaos in a simple model of shear banding, Phys. Rev. Lett. 92 (2004) 084502.
[13] E.S. Boek, J.T. Padding, V.J. Anderson, P.M.J. Tardy, J.P. Cranshaw, J.R.A. Pearson, Constitutive equations for extensional flow of wormlike micelles: stability analysis of the Bautista–Manero model, J. Non-Newton. Fluid Mech. 126 (2005) 39–46.
[14] V.J. Anderson, J.R.A. Pearson, E.S. Boek, The Rheology of wormlike micellar fluids, Rheol. Rev. 2006 (2006) 217–254.
[15] G. Pickard, a. Adjari, L. Bocquet, F. Lequeux, Simple model for heterogeneous flows of yield stress fluids, Phys. Rev. E 66 (2002) 051501.
[16] F. Bautista, M. Muñoz, J. Castillo-Tejas, J.H. Pérez-López, J.E. Puig, O. Manero, Critical phenomenon analysis of shear-banding flow in polymer-like micellar solutions. 1. Theoretical approach, J. Phys. Chem. B 113 (2009) 16101–16109.
[17] O. Manero, J.H. Pérez-López, J.I. Escalante, J.E. Puig, F. Bautista, A thermodynamic approach to rheology of complex fluids: the generalized BMP model, J. Non-Newton. Fluid Mech. 146 (2007) 22–29.
[18] S.M. Fielding, Vorticity structuring and velocity rolls triggered by gradient shear bands, Phys. Rev. E 76 (2007) 016311.
[19] C.A. Smith, A. Corripio, Principles and Practice of Automatic Process Control, third ed., John Wiley & Sons, 2006.
[20] P.D. Olmsted, Perspectives on shear banding in complex fluids, Rheol. Acta 47 (2008) 283–300.
[21] X.-F. Yuan, L. Jupp, Interplay of flow-induced phase separations and rheological behavior of complex fluids in shear banding flow, Europhys. Lett. 60 (2002) 691–697.
[22] S. Manneville, A. Colin, G. Waton, F. Schosseler, Wall slip, shear banding, and instability in the flow of a triblock copolymer micellar solution, Phys. Rev. E 75 (2007) 061502.
[23] S. Lerouge, J.-P. Decruppe, P. Olmsted, Birefringence banding in a micellar solution or the complexity of heterogeneous flows, Langmuir 20 (2004) 11355–11365.
[24] E. Miller, J.P. Rothstein, Transient evolution of shear banding in wormlike micellar solutions, J. Non-Newton. Fluid Mech. 143 (2007) 22–37.
[25] R. Courant, D. Hilbert, Methods of mathematical physics, Partial Differential Equations, vol. II, Wiley, New York, 1962.
[26] H.-K. Rhee, R. Aris, N. Amundson, First-order partial differential equations, Theory and Applications of Single Equations, vol. 1, Dover, New York, 1989.
[27] H.-K. Rhee, R. Aris, N. Amundson, First-order partial differential equations, Theory and Applications of Hyperbolic Systems of Quasilinear Equations, vol. 2, Dover, New York, 1989.